

# Model error in the LANS-alpha and NS-alpha deconvolution models of turbulence

Eric Olson\*

June 20, 2017

## Abstract

This paper reports on a computational study of the model error in the LANS-alpha and NS-alpha deconvolution models of homogeneous isotropic turbulence. Computations are also performed for a new turbulence model obtained as a rescaled limit of the deconvolution model. The technique used is to plug a solution obtained from direct numerical simulation of the incompressible Navier–Stokes equations into the competing turbulence models and to then compute the time evolution of the resulting residual. All computations have been done in two dimensions rather than three for convenience and efficiency. When the effective averaging length scale in any of the models is  $\alpha_0 = 0.01$  the time evolution of the root-mean-squared residual error grows as  $\sqrt{t}$ . This growth rate similar to what would happen if the model error were given by a stochastic force. When  $\alpha_0 = 0.20$  the residual error grows linearly. Linear growth suggests that the model error possesses a systematic bias. Finally, for  $\alpha_0 = 0.04$  the residual error in LANS-alpha model exhibited linear growth; however, for this value of  $\alpha_0$  the higher-order alpha models that were tested did not.

## 1 Introduction

Consider two dynamical systems

$$\frac{du}{dt} = \mathcal{F}(u) \quad \text{and} \quad \frac{dv}{dt} = \tilde{\mathcal{F}}(v)$$

on a Hilbert space  $V$  with norm  $\|\cdot\|$ . Suppose the evolution of  $u$  is given by exact dynamics and the evolution of  $v$  according to some approximate dynamics. Define the model error of the approximate dynamics as the residual  $R$  obtained by plugging the exact solution  $u$  into the equation governing  $v$ . Thus,

$$dR = du - \tilde{\mathcal{F}}(u)dt = (\mathcal{F}(u) - \tilde{\mathcal{F}}(u))dt \tag{1}$$

---

\*Department of Mathematics and Statistics, University of Nevada, Reno, NV 89557, USA. *email:* ejolson@unr.edu

where by convention we take  $R(0) = 0$ . Specifically, consider the case where  $\mathcal{F}$  is given by the two-dimensional incompressible Navier–Stokes equations and  $\tilde{\mathcal{F}}$  represents a particular alpha turbulence model. The focus of this paper is whether, to what extent, and under what conditions do the residuals  $R$  obtained through numeric computation behave qualitatively as spatially-correlated and temporally-white Gaussian processes.

This question is motivated, in part, by the analysis of Hoang, Law and Stuart [20] for the 4DVAR data assimilation algorithm. That analysis assumes  $R = W$  where  $W$  is a spatially-correlated and temporally-white Gaussian process and proceeds to show that the inverse problem of finding the initial condition  $u_0$  and the posterior distribution of  $W$  is a continuous function of noisy observations of the velocity field. In light of this result, we are interested whether the assumption  $R = W$  is realistic when the residual error is given by actual turbulence models. We are also motivated by the simple desire to compare different turbulence models. Stolz, Adams and Kleiser [33] state that taking the order for the NS-alpha deconvolution models to be  $d = 3$  already gives acceptable results while choosing the order larger than 5 does not improve the results significantly. We test this claim by examining the growth rate of  $R$  for different values of  $d$  and comparing the results to a new rescaled limit of the deconvolution model which has an exponentially small consistency error.

The LANS-alpha model of turbulence is given by the equations

$$\begin{aligned} \frac{\partial v}{\partial t} + (\bar{v} \cdot \nabla)v + v_j \nabla \bar{v}_j &= \nu \Delta v - \nabla p + f, \\ \nabla \cdot \bar{v} &= 0 \quad \text{where} \quad v = (1 - \alpha^2 \Delta)\bar{v}. \end{aligned} \tag{2}$$

Here  $v$  is the Eulerian velocity field,  $\bar{v}$  is the average velocity field,  $\alpha$  is the averaging length scale,  $\nu$  is the kinematic viscosity,  $p$  is the physical pressure and  $f$  is a body force. Note that setting  $\alpha = 0$  yields the standard Navier–Stokes equations. These equations, originally called the viscous Camassa–Holm equations, were introduced as a closure for the Reynolds averaged Navier–Stokes equations by Chen, Foias, Holm, Olson, Titi and Wynne in 1998 through a series of papers [4, 5, 6]. At the same time, numerical simulations by Chen, Holm, Margolin and Zhang [7] concluded that the LANS-alpha model also functions as an effective subgrid-scale model. Connections to the theory of global attractors and homogeneous isotropic turbulence and global attractors appear in [14].

Note that equations (2) can be derived as the Euler-Poincaré equations of an averaged Lagrangian to which a viscous term, obtained by identifying the momentum in the physical derivation, has been added. This derivation further assumes that the turbulence is homogeneous and isotropic. A body of theoretical and numerical literature on the LANS- $\alpha$  model exists—see [3, 8, 10, 18, 20, 21, 24, 25, 26] and references therein—that, among other things, explores the dependency on  $\alpha$  and the limit when  $\alpha \rightarrow 0$ , relaxes the homogeneity and isotropy assumptions, studies boundary conditions and boundary layers, and treats other physical systems. In summary, the LANS-alpha model is a well-studied turbulence model that is suitable for further study here.

To avoid a study of boundary layers we consider flows in domains with periodic boundary conditions. To approximate homogeneous and isotropic turbulence we choose a time-independent body forcing that has no regular patterns in space and for which the resulting flow undergoes complex time dependent behavior that in no way resembles the force, see

Figure 3. Since the body-force is time independent, it is natural to suppose the statistics of the flow are stationary. While these assumptions are consistent with the classical theories of fully developed turbulence developed by Kolmogorov [29] and Kraichnan [30], the possibility of intermittency may lead to non-equilibrium and non-stationarity. Moreover, while domains with periodic boundary conditions are obviously homogeneous, the presence of any non-zero forcing function has the potential to render the statistics of the resulting flow inhomogeneous. As noted by Kurien, Aivalis and Sreenivasan [31], see also Taylor, Kurien and Eyink [34], even when the body forcing is zero, turbulent flows in periodic domains can possess a certain degree of anisotropy. It is hoped, therefore, that the stationarity, homogeneity and isotropy assumptions made in the derivation of the LANS-alpha and NS-alpha deconvolution models are well enough satisfied that the turbulence models studied here apply. Viewed in a different way, our computations of the residual error may be seen as a test of these assumptions.

The NS-alpha deconvolution model of turbulence is structurally the same as the LANS-alpha model, except that the derivation allows for the more general filtering relationship between  $v$  and  $\bar{v}$  given by

$$\bar{v} = D_d(I - \alpha^2\Delta)^{-1}v \quad (3)$$

where  $D_d$  is the  $d$ -th order van Cittert approximate deconvolution operator

$$D_d = \sum_{n=0}^d (1 - (1 - \alpha^2\Delta)^{-1})^n.$$

Note that setting  $d = 0$  yields the LANS-alpha model and setting  $\alpha = 0$  again yields the incompressible Navier–Stokes equations. This model was introduced by Rebholz [28] as a helicity correction to higher-order Leray-alpha models. It may also be seen as the  $\alpha = \beta$  case of the alpha-beta models which have been the subject of recent numerical work by Kim, Neda, Rebholz and Fried [22] and others. For simplicity we don't consider the alpha-beta generalization here, but instead focus solely on how the order  $d$  of the deconvolution operator affects the growth of the residual error.

In this paper we also study the limit turbulence model obtained by identifying the effective averaging length scale  $\alpha_0 = \alpha/\sqrt{d+1}$  in the NS-alpha deconvolution model and then taking  $d \rightarrow \infty$  while holding  $\alpha_0$  constant. This results in a new turbulence model with an exponential smoothing filter given by

$$\bar{v} = \left\{1 - \exp\left(\frac{\Delta^{-1}}{\alpha_0^2}\right)\right\}v$$

with the same structure as LANS-alpha and NS-alpha deconvolution models. For convenience of terminology in the remainder of this paper, we will refer to this limit turbulence model as the *exponential-alpha model*.

Since the dynamics of the turbulence models considered here are deterministic, the model error represented by the residual  $R$  is also deterministic. To understand to what extent our computations support the assumptions in [20], we now recall what happens when the model error is actually equal to a stochastic force and further what happens when it contains a systematic bias. Suppose  $\tilde{\mathcal{F}}(u)dt = \mathcal{F}(u)dt - dW$  where  $W$  is a  $V$ -valued  $Q$ -Brownian motion. Here  $V$  is an infinite dimensional Hilbert space and  $Q$  is a trace-class symmetric

linear operator on  $V$ . Let  $\Xi$  be the underlying probability space. For each  $\xi \in \Xi$  we obtain a residual realized by the sample path  $R(t) = W(t; \xi)$ . Thus,

$$\mathbf{E}[\|R(t)\|^2] = \text{Tr} [\text{Cov}(R(t))] = t \text{Tr } Q.$$

If the model error also contains a systematic bias, then

$$R(t) = tF_b + W(t; \xi) \tag{4}$$

where  $F_b \in V$  is the bias. In this case,

$$\mathbf{E}[\|R(t)\|^2] = t^2\|F_b\|^2 + t \text{Tr } Q. \tag{5}$$

Note that the root-mean-squared residual error  $\mathcal{E}_{\text{rms}}(t) = \mathbf{E}[\|R(t)\|^2]^{1/2}$  grows as  $\sqrt{t}$  in the stochastic case and linearly when there is systematic bias.

Returning now to the deterministic case, let  $\mathcal{F}$  represent the dynamics of the two-dimensional incompressible Navier–Stokes equations and  $\tilde{\mathcal{F}}$  be the two-dimensional version of one of the alpha turbulence models described above. As we are studying fully developed turbulence that arises from long-term evolution, it is reasonable to suppose  $u_0$  lies on the global attractor  $\mathcal{A}$  determined by the exact dynamics. We further assume, for computational convenience, that all our solutions are  $2\pi$ -periodic with mean zero.

Thus, for each  $u_0 \in \mathcal{A}$  we obtain a solution  $u(t, x)$  to the incompressible two-dimensional Navier–Stokes equations of the form

$$u(t, x) = \sum_{k \in \mathbf{Z}^2 \setminus \{0\}} u_k(t) e^{ik \cdot x} \quad \text{with} \quad u_k(t) \in \mathbf{C}^2$$

such that  $u_k = \overline{u_{-k}}$  and  $k \cdot u_k = 0$ . Foias and Temam show in [12], that such solutions are analytic in time with values in a Gevrey class of functions. This implies, see also [15, 35] and references therein, that there exist constants  $M_\alpha$  depending only on  $\nu$  and  $f$  such that

$$\|u\|_\alpha^2 = ((u, u))_\alpha \leq M_\alpha \quad \text{where} \quad ((u, v))_\alpha = 4\pi^2 \sum_{k \in \mathcal{J}} |k|^{2\alpha} u_k \overline{v_k}$$

for all  $t \in \mathbf{R}$  and  $u_0 \in \mathcal{A}$ . For notational convenience write  $\|u\| = \|u\|_1$  and  $((u, v)) = ((u, v))_1$ . We take  $V = \{u : \|u\| < \infty\}$  note that  $R(t; u_0) \in V$  and also that the divergence-free condition implies this norm is equivalent to the  $H^1$  Sobolev norm.

The residual  $R$  depends on the solution  $u$  to the exact dynamics, which in turn, depends on the initial condition  $u_0$ . Since  $u_0$  is unknown in the case of data assimilation, we may interpret the parameter  $\xi$  in (4) as depending on an unknown  $u_0 \in \mathcal{A}$  distributed according some probability measure  $\mu$ . This leads to a natural definition of the root-mean-square residual error using ensemble averages as

$$\mathcal{E}_{\text{rms}}(t) = \langle \|R(t)\|^2 \rangle^{1/2} = \left\{ \int_{\mathcal{A}} \|R(t; u_0)\|^2 d\mu(u_0) \right\}^{1/2}. \tag{6}$$

We are now able to state one of our main results: *If  $\alpha_0$  is sufficiently small, then numerical computations show  $\mathcal{E}_{\text{rms}}(t)$  grows as  $\sqrt{t}$ ; however, if  $\alpha_0$  is too large, then  $\mathcal{E}_{\text{rms}}(t)$  grows linearly in time. Moreover, even before taking ensemble averages our computations show for each of*

the hundred different  $u_0 \in \mathcal{A}$  tested that  $\|R(t; u_0)\|$  grows as  $\sqrt{t}$  when  $\alpha_0$  is sufficiently small and linearly when  $\alpha_0$  is large.

Of course the computational fact that  $\mathcal{E}_{\text{rms}}(t)$  grows as  $\sqrt{t}$  for small values of  $\alpha_0$  does not imply the model errors in the corresponding alpha models are actually given by Brownian motions. Brownian motions have independent increments and are almost-surely nowhere differentiable. On the other hand the deterministic residuals studied here are differentiable and, as will briefly be shown, do not have independent increments.

Given  $\delta > 0$  define  $Z_j = Z(\tau_j, \delta)$  where

$$\tau_j = j\delta \quad \text{and} \quad Z(t, \delta) = R(t; u_0) - R(t - \delta; u_0). \quad (7)$$

If the residual errors had independent increments then we would have  $\langle Z_j \otimes Z_{j+1} \rangle = 0$  for any value of  $\delta$ . The following argument shows this is not the case provided  $\delta$  is small enough. Consider the function  $r(t) = \langle (R(t; u_0), \phi) \rangle$  where  $\phi \in V$ . In light of the analyticity of  $u(t)$ , the function  $r(t)$  is continuously differentiable with time derivatives that are uniformly bounded on the attractor. Thus, for  $l = 0, 1, 2, \dots$  we have

$$B_l = \sup\{|r^{(l)}(t)| : u_0 \in \mathcal{A}, \|\phi\| = 1 \text{ and } t \in \mathbf{R}\} < \infty.$$

Although  $r'(t)$  may vanish for some choices of parameters, it is reasonable to suppose that the ensemble average of  $r'(t)^2$  is positive.

In particular, we assume there exists  $\epsilon > 0$  and  $T > 0$  such that

$$\sup\{\langle r'(t)^2 \rangle^{1/2} : \|\phi\| = 1\} \geq \epsilon \quad \text{for all } t \in [0, T]. \quad (8)$$

While (8) is satisfied with  $T = 100\,000$  in each of our computations as seen in Table 1, a rigorous justification is outside the scope of the present work. Intuitively, such a justification would depend on the support of  $\mu$  including points which are not fixed points. If the support consists of points whose trajectories are chaotic, then plausibly (8) could hold for all  $t \in \mathbf{R}$ . While we do not need this stronger condition, we note for the choice of parameters considered in our computations that the long term evolution depicted in Figure 3 does indeed suggest that the attractor consists of chaotic trajectories.

By Taylor's theorem we have

$$\begin{aligned} r(\tau_{j-1}) &= r(\tau_j) - \delta r'(\tau_j) + \frac{1}{2}\delta^2 r''(c_1) \\ r(\tau_{j+1}) &= r(\tau_j) + \delta r'(\tau_j) + \frac{1}{2}\delta^2 r''(c_2) \end{aligned}$$

where  $\tau_{j-1} < c_1 < \tau_j < c_2 < \tau_{j+1}$ . It follows from the mean value theorem that

$$\begin{aligned} (Z_j \otimes Z_{j+1})(\phi, \phi) &= (r(\tau_j) - r(\tau_{j-1}))(r(\tau_{j+1}) - r(\tau_j)) \\ &= \delta^2 \{r'(\tau_j)^2 + \frac{1}{2}\delta r'(\tau_j)(r''(c_2) - r''(c_1)) - \frac{1}{2}\delta^2 r''(c_1)r''(c_2)\} \\ &= \delta^2 \{r'(\tau_j)^2 + \frac{1}{2}\delta(c_2 - c_1)r'(\tau_j)r'''(c_3) - \frac{1}{2}\delta^2 r''(c_1)r''(c_2)\} \\ &\geq \delta^2 \{r'(\tau_j)^2 - \delta^2 M^2\} \end{aligned}$$

where  $M^2 = B_1 B_3 + \frac{1}{2}B_2^2$ . Now, choosing  $\delta \leq \min\{T, 2^{-1/2}\epsilon/M\}$  yields

$$\sup\{\langle (Z_1 \otimes Z_2)(\phi, \phi) \rangle : \|\phi\| = 1\} \geq \delta^2 \{\epsilon^2 - \delta^2 M^2\} \geq \frac{1}{2}\delta^2 \epsilon^2 > 0. \quad (9)$$

Therefore, the increments are positively correlated provided  $\delta$  is small enough.

Although the residual error in a deterministic turbulence model does not consist of independent increments, for the choice of flow-parameters considered here the fact that solutions to the Navier–Stokes equations have a sensitive dependence on initial conditions and seem to forget their initial conditions exponentially over time leads to the possibility that the increments may appear independent when  $\delta$  is large. In general, chaotic systems can produce time-series that are indistinguishable from Gaussian random noise when analyzed with any type of linear analysis—power spectrum, autocorrelation or probability distribution functions—see, for example, Sprott [32]. Therefore, instead of performing standard statistical tests often used to check for randomness in economic data such as the Ljung–Box  $Q$ -statistic [2] or the variance-ratio test of Lo and MacKinlay [23], we instead content ourselves with some simple descriptive statistics.

This paper is organized as follows: Section 2 explores the relation between  $\alpha$  and  $d$  in the NS-alpha deconvolution model to show that the effective averaging length scale  $\alpha_0$  depends on  $d$  as  $\alpha_0 = \alpha/\sqrt{d+1}$ . We then derive the exponential alpha model by taking the limit  $d \rightarrow \infty$  while holding  $\alpha_0$  fixed. Section 3 describes the numerical methods used to compute the solution  $u$  of the two-dimensional incompressible Navier–Stokes equations that will be plugged into the turbulence models to compute the residual error. In Lemma 1 we show for small enough time steps that the resulting discrete dynamical system posses a global attractor. Section 4 presents our computational results including our main result on the growth rate of  $\mathcal{E}_{\text{rms}}(t)$ . Section 5 further describes the statistical properties of residual error. The paper ends by summarizing our conclusions and stating some plans for future work.

## 2 The Effective Averaging Length Scale

In this section we identify the effective averaging length scale in the NS-alpha deconvolution model as  $\alpha_0 = \alpha/\sqrt{d+1}$  and then use this identification to derive the exponential-alpha model as the limit  $d \rightarrow \infty$  holding  $\alpha_0$  constant. Any deconvolution model based on the smoothing filter  $(1 - \alpha^2\Delta)^{-1}$  will have the same scaling between  $\alpha$  and  $\alpha_0$  and exponential-alpha model in the limit. In particular, the effective averaging length scale  $\alpha_0$  identified here applies equality well to three-dimensional fluid flows.

We consider the effects of the smoothing filter (3) on regular  $2\pi$ -periodic functions with zero spatial average in Fourier space. Similar results could be obtained in more general settings, however, since our computations will be made for  $2\pi$ -periodic domains, it is easiest to work in that setting from the beginning. Henceforth, write the functions  $v$  and  $\bar{v}$  in terms of Fourier series as

$$v(x, t) = \sum_{k \in \mathbf{Z}^2 \setminus \{0\}} v_k(t) e^{ik \cdot x} \quad \text{and} \quad \bar{v}(x, t) = \sum_{k \in \mathbf{Z}^2 \setminus \{0\}} \bar{v}_k(t) e^{ik \cdot x}.$$

It follows the smoothing filter (3) in the NS-alpha deconvolution model may be written as

$$\bar{v}_k = D_{d,k} (1 - \alpha^2 |k|^2)^{-1} v_k$$

where

$$D_{d,k} = \sum_{n=0}^d \left(1 - \frac{1}{1 + \alpha^2 |k|^2}\right)^n = \sum_{n=0}^d \left(\frac{\alpha^2 |k|^2}{1 + \alpha^2 |k|^2}\right)^n.$$

Summing the above geometric series yields

$$\frac{D_{d,k}}{1 + \alpha^2|k|^2} = 1 - \left( \frac{\alpha^2|k|^2}{1 + \alpha^2|k|^2} \right)^{d+1}.$$

Observe that

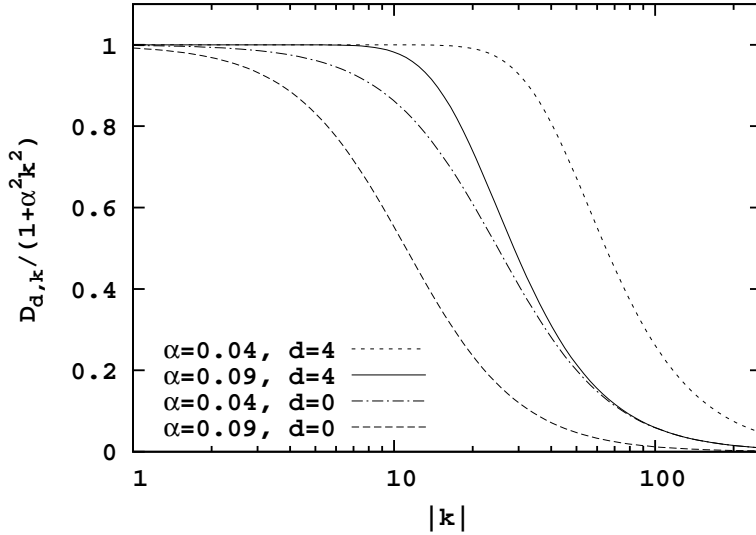
$$\frac{D_{d,k}}{1 + \alpha^2|k|^2} \rightarrow 1 \quad \begin{array}{l} \text{as } d \rightarrow \infty \text{ holding } \alpha \text{ constant,} \\ \text{or as } \alpha \rightarrow 0 \text{ holding } d \text{ constant.} \end{array}$$

At the same time, note that

$$\frac{D_{d,k}}{1 + \alpha^2|k|^2} \rightarrow 0 \quad \text{as } \alpha \rightarrow \infty \text{ holding } d \text{ constant.}$$

The above limits suggest there may be a tradeoff between  $\alpha$  and  $d$  which could be used to identify an effective averaging length scale  $\alpha_0$  that depends on  $d$ .

Figure 1: The smoothing filter in the NS-alpha deconvolution model in Fourier space for four different choices of  $\alpha$  and  $d$ .



Evidence of such a tradeoff is presented in Figure 1 where four representative curves of the smoothing filter  $D_{d,k}/(1 + \alpha^2|k|^2)$  are plotted for  $\alpha \in \{0.04, 0.09\}$  and  $d \in \{0, 4\}$ . Smaller values of  $\alpha$  lead to a smoothing filter which is closer to 1 while larger values of  $d$  also yield a filter which is closer to 1. Moreover, the high-frequency attenuation is nearly the same when  $\alpha = 0.09$  and  $d = 4$  as it is when  $\alpha = 0.04$  and  $d = 0$ . This suggests a clear tradeoff between  $d$  and  $\alpha$  for which the microscales are the same.

We now perform an asymptotic analysis of  $D_{d,k}/(1 + \alpha^2|k|^2)$  as  $k \rightarrow \infty$  to precisely identify the effective averaging length scale  $\alpha_0$  that leaves the high-frequency attenuation of the smoothing filter unchanged as  $d$  is varied. Since

$$\frac{D_{d,k}}{1 + \alpha^2|k|^2} = 1 - \left( \frac{\alpha^2|k|^2}{1 + \alpha^2|k|^2} \right)^{d+1} \sim \frac{d+1}{\alpha^2|k|^2} \quad \text{as } k \rightarrow \infty,$$

one can rescale the filter by setting  $\alpha = \alpha_0 \sqrt{d+1}$  where  $\alpha_0$  is constant to obtain an asymptotic decay that is independent of  $d$  when  $k \rightarrow \infty$ . The fact that  $0.09 \approx 0.04 \sqrt{4+1}$  now explains why the high-frequency attenuation was nearly the same for two of the curves in Figure 1.

The above identification motivates the definition of the rescaled smoothing filter  $H_{d,k}$  in terms of the effective averaging length scale  $\alpha_0$  as

$$H_{d,k} = \frac{D_{d,k}}{1 + (d+1)\alpha_0^2|k|^2} = 1 - \left( \frac{(d+1)\alpha_0^2|k|^2}{1 + (d+1)\alpha_0^2|k|^2} \right)^{d+1}.$$

The limit  $d \rightarrow \infty$  holding  $\alpha_0$  constant now leads to the non-trivial limit filter

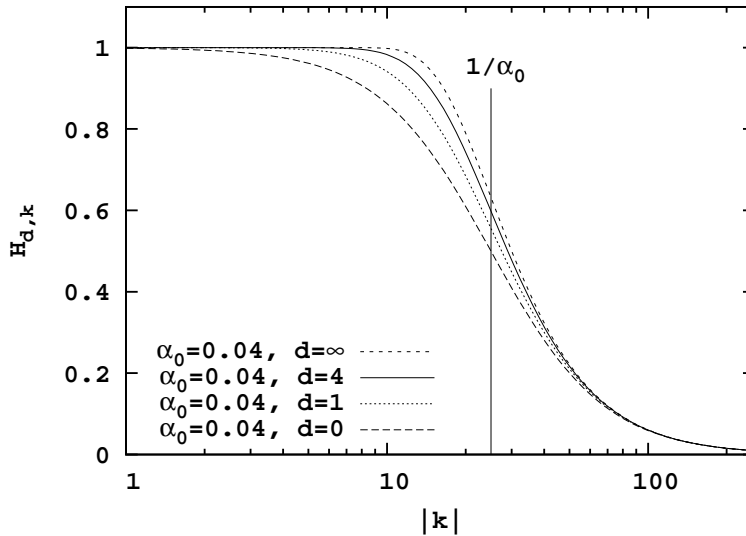
$$H_{\infty,k} = 1 - \lim_{d \rightarrow \infty} \left( \frac{(d+1)\alpha_0^2|k|^2}{1 + (d+1)\alpha_0^2|k|^2} \right)^{d+1} = 1 - \exp\left(\frac{-1}{\alpha_0^2|k|^2}\right).$$

Moreover, for every  $d \in \mathbf{N} \cup \{\infty\}$  we have that

$$H_{d,k} \sim \frac{1}{\alpha_0^2|k|^2} \quad \text{as} \quad k \rightarrow \infty$$

and therefore the high-frequency attenuation of this family of filters is independent of  $d$ . Figure 2 demonstrates how changing  $d$  affects  $H_{d,k}$  in the low modes without affecting the microscales.

Figure 2: When  $\alpha_0$  is fixed the cutoff for the high modes is independent of the order  $d$ . The vertical line denotes  $|k| = 1/\alpha_0$ .



We remark that this is the first time the exponential filter  $H_{\infty,k}$  has been derived and proposed for use in the context of turbulence modeling. A Gaussian filter of the form  $\exp(-\alpha_0^2|k|^2)$  was considered for the Leray and LANS-alpha models by Geurts and Holm [17]. That filter is a mirror-image reflection of the one derived here: Instead of preserving the cutoff in the high modes, it holds fixed the  $d = 0$  order of the low modes.



For smooth functions  $u$  the filters  $H_{d,k}$  have a consistency error given by

$$u - H_{d,k}u = \begin{cases} \mathcal{O}(\alpha_0^{2d+2}) & \text{for } d \in \mathbf{N} \\ \mathcal{O}(\exp(-1/\lambda_0\alpha_0^2)) & \text{for } d = \infty \end{cases} \quad \text{as } \alpha_0 \rightarrow 0$$

where  $\lambda_0$  is the smallest eigenvalue of the Stokes operator. Therefore, the consistency error as a function of the effective averaging length scale  $\alpha_0$  is the same as the results proved by Stolz, Adams and Kleiser [33], see also Dunca and Epshteyn [11], for the NS-alpha deconvolution model. Moreover, the exponential filter obtained in the limit when  $d \rightarrow \infty$  has exponentially small consistency error as  $\alpha_0 \rightarrow 0$ . We turn now to our computational results.

### 3 Numerical Methods

The vorticity formulations of the Navier–Stokes equations and the turbulence models described in the introduction are particularly simple in two dimensions. Using the notation  $\text{curl } u = \partial u_2/\partial x_1 - \partial u_1/\partial x_2$ , the two-dimensional incompressible Navier–Stokes equations can be expressed as the scalar equation

$$\frac{\partial \omega}{\partial t} - \nu \Delta \omega + u \cdot \nabla \omega = g \quad \text{where} \quad \omega = \text{curl } u \quad (10)$$

and  $g = \text{curl } f$ . Similarly, the alpha turbulence models are all given by

$$\frac{\partial m}{\partial t} - \nu \Delta m + \bar{v} \cdot \nabla m = g \quad \text{where} \quad H_d m = \text{curl } \bar{v} \quad (11)$$

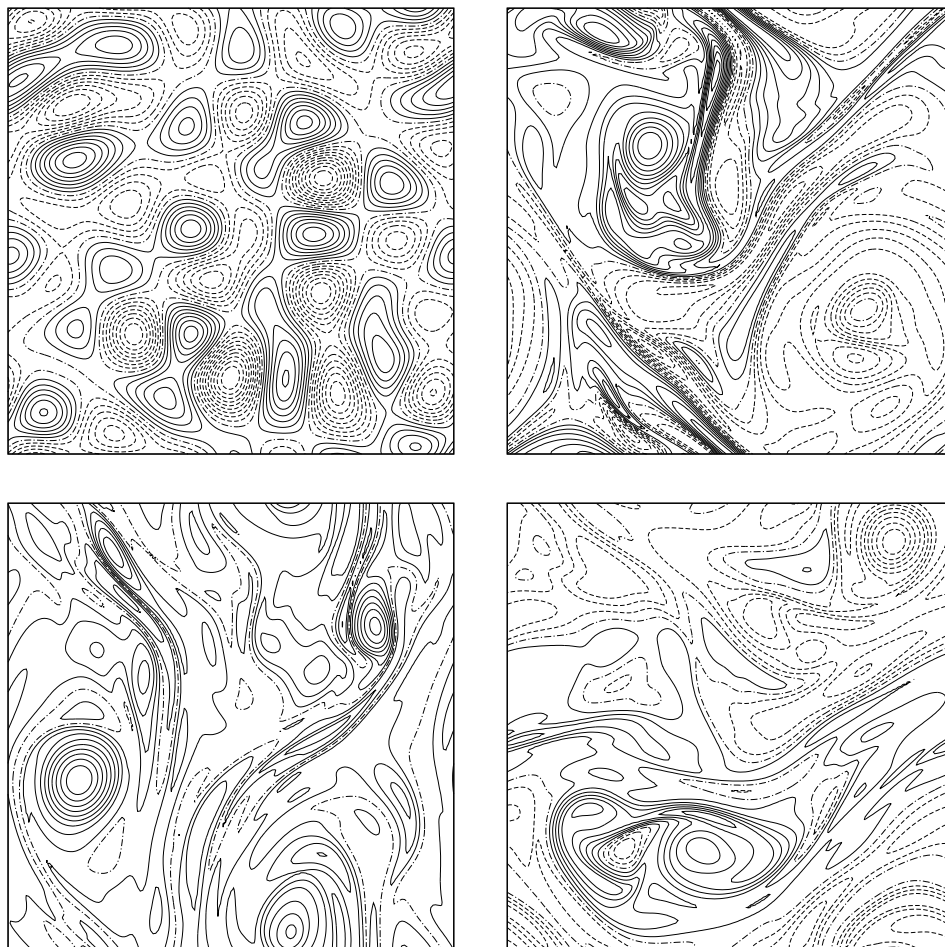
and  $H_d$  is the differential operator corresponding to the symbol  $H_{d,k}$  in the previous section. We recall equations (11) reduce to the LANS-alpha model when  $d = 0$  and that the new exponential-alpha model is obtained when  $d = \infty$ .

It is well known, see for example Temam [35], that the two-dimensional Navier–Stokes equations are well-posed. That is, these equations possess unique smooth solutions depending continuously on the initial conditions provided the force is sufficiently regular. Foias, Holm and Titi [13] show that three-dimensional LANS-alpha model is also well posed. It follows, trivially, that the two-dimensional LANS-alpha model is well posed. Similar results hold for NS-alpha deconvolution model and also for the new exponential-alpha model.

We shall consider a two-dimensional incompressible flow in a  $2\pi$ -periodic box forced by a  $2\pi$ -periodic body force. Specifically, take  $\Omega = [0, 2\pi]^2$ , the viscosity  $\nu = 0.0001$  and choose a time-independent divergence-free body forcing  $f$  supported on the Fourier modes with  $16 \leq |k|^2 \leq 34$  such that  $\|f\|_{L^2} = 0.0025$  and for which the Grashof number is  $G = \nu^{-2}\|f\|_{L^2} = 250\,000$ . To obtain such a force, the amplitudes of the Fourier modes were chosen randomly and then rescaled to obtain the desired Grashof number. The exact function used here is depicted top left in Figure 3 and originally appeared in Olson and Titi [27] where it was called  $f_{25}$  to indicate its support lied on an annulus about  $|k|^2 = 25$  in Fourier space.

Since we have written our fluid equations in vorticity form, it is natural to compute the residual vorticity  $\rho$  given by  $\rho = \text{curl } R$ . No generality is lost in doing this, because we may later recover  $R$  by inverting the definition of  $\rho$  subject to the condition  $\nabla \cdot R = 0$ . Note, as

Figure 3: Top left shows the contours of the force  $g = \text{curl } f$ ; in order following are contours of  $\omega$  at times 25 000, 50 000 and 100 000.



the velocity fields present in both the exact and approximate dynamics are divergence free, so  $R$  is divergence free. Therefore, we plug  $\omega$  into equation (11) to obtain

$$d\rho = ((\bar{u} \cdot \nabla \omega) - (u \cdot \nabla \omega))dt.$$

Integrating in time then yields

$$\rho(t) = \int_0^t ((\bar{u} \cdot \nabla \omega) - (u \cdot \nabla \omega))dt. \quad (12)$$

It is worth remarking that at no point does the time evolution of the approximate dynamics (11) governing  $m$  enter into the computation of  $\rho$ . Indeed, sensitive dependence on initial conditions is well known for the dynamical systems studied here, which in turn, implies there is no shadowing result that could be used to compare separate evolutions of  $\omega$  and  $m$  over long periods of time.

Theoretically the evolution of  $\omega$  should be determined by the exact dynamics of the two-dimensional incompressible Navier–Stokes equations. As this is not possible in any numerical

experiment, we therefore consider two discrete dynamical systems

$$\omega^{n+1} = S(\omega^n) \quad \text{and} \quad m^{n+1} = \tilde{S}(m^n)$$

and suppose the discrete dynamics of  $\omega^n$  are exact while  $m^n$  evolves according to some approximate dynamics. The discrete model error in the approximate dynamics is then given by the residual

$$\rho^{n+1} = \rho^n + S(\omega^n) - \tilde{S}(\omega^n) \quad \text{where} \quad \rho^0 = 0. \quad (13)$$

Note that since (13) represents an exact definition at the discrete level, we obtain a method of computing the model error in the corresponding discrete alpha models to within the precision of the available floating-point arithmetic.

In the computations presented here the discrete solution  $\omega^n$ , which we view as being governed by the exact dynamics, shall be given by the fully-dealiased spectral Galerkin method for approximating equations (10) in which the linear terms have been integrated exactly in time and the nonlinear term using an Euler method. In particular, given  $K \in \mathbf{N}$  fixed, let

$$\mathcal{K} = \{ (k_1, k_2) \in \mathbf{Z}^2 \setminus \{0\} : -K \leq k_1, k_2 \leq K \}$$

and write

$$\omega^n(x) = \sum_{k \in \mathcal{K}} \omega_k^n e^{ik \cdot x} \quad \text{and} \quad u^n(x) = \sum_{k \in \mathcal{K}} \frac{i(k_2, -k_1)}{|k|^2} \omega_k^n e^{ik \cdot x}.$$

By definition, then, the exact dynamics are given by

$$\omega^{n+1} = S(\omega^n) \quad \text{for} \quad n = 0, 1, 2, \dots \quad (14)$$

where the discrete semigroup operator  $S$  is given by

$$\begin{aligned} S(\omega^n)_k &= \left\{ \omega_k^n - h(u^n \cdot \nabla \omega^n)_k \right\} e^{-\nu|k|^2 h} \\ &\quad + \frac{2g_k}{\nu|k|^2} e^{-\nu|k|^2 h/2} \sinh(\nu|k|^2 h/2). \end{aligned} \quad (15)$$

While  $S$  acts on the vorticity, an equivalent semigroup may be defined which acts on the velocity. For notational simplicity we shall refer to both semigroups as  $S$ . Thus  $u^{n+1} = S u^n$  shall mean  $u^{n+1} = \text{curl}^{-1} S \text{curl} u^n$ .

The corresponding approximate dynamics of our discrete alpha models are given by

$$m^{n+1} = \tilde{S}(m^n) \quad \text{for} \quad n = 0, 1, 2, \dots \quad (16)$$

where

$$m^n = \sum_{k \in \mathcal{K}} m_k^n e^{ik \cdot x}, \quad \bar{v}^n = \sum_{k \in \mathcal{K}} \frac{i(k_2, -k_1)}{|k|^2} H_{d,k} m_k^n e^{ik \cdot x}$$

and

$$\begin{aligned} \tilde{S}(m^n)_k &= \left\{ m_k^n - h(\bar{v}^n \cdot \nabla m^n)_k \right\} e^{-\nu|k|^2 h} \\ &\quad + \frac{2g_k}{\nu|k|^2} e^{-\nu|k|^2 h/2} \sinh(\nu|k|^2 h/2). \end{aligned}$$

Note that  $\omega_k^n$  may be viewed as a discrete approximation of the continuous solution  $\omega$  to equations (10) projected onto the Fourier mode  $\exp(ik \cdot x)$  at time  $t_n = hn$  for some time step  $h > 0$  and  $m_k^n$  may be viewed as an identically discretized approximation of the solution  $m$  given by an alpha model. Although more accurate and stable time stepping methods could be used, the above is sufficient for our present study.

We now prove for  $K$  fixed and  $h$  small enough that the discrete dynamical system (14) possesses a unique global attractor  $\mathcal{A}_{K,h}$ . This follows directly from following lemma which shows the existence of an absorbing ball. In order to keep track of the dimensional quantities which appear in the proof, define

$$\lambda_0 = \min\{|k|^2 : k \in \mathcal{K}\} = 1$$

and recall that  $g_k = 0$  for  $|k|^2 > \lambda_M$  where  $\lambda_M = 34$ .

**Lemma 1** *Let*

$$B = c_0 \frac{\|f\|_{L^2}}{\nu \lambda_0^{1/2}} \quad \text{where} \quad c_0 > 6\lambda_M/\lambda_0.$$

*Given  $K$  fixed and  $L > 0$ , there is  $h$  small enough and  $N$  large enough such that  $|w^0| < L$  implies  $|w^n| < B$  for all  $n \geq N$ .*

*Proof.* From (14) we have

$$\omega_k^{n+1} e^{\nu|k|^2 h} = \omega_k^n - h(u^n \cdot \nabla \omega^n)_k + \frac{2g_k}{\nu|k|^2} (e^{\nu|k|^2 h} - 1).$$

Therefore

$$\sum_{k \in \mathcal{K}} \omega_k^{n+1} e^{\nu|k|^2 h} e^{ik \cdot x} = \omega^n - h(u^n \cdot \nabla \omega^n) + \sum_{k \in \mathcal{K}} \frac{2g_k}{\nu|k|^2} (e^{\nu|k|^2 h} - 1) e^{ik \cdot x}.$$

Let

$$|\omega^n|^2 = \|\omega^n\|_{L^2}^2 = 4\pi^2 \sum_{k \in \mathcal{K}} |\omega_k^n|^2.$$

Since all norms are equivalent in finite dimensions spaces, then there exists  $C_K$  such that  $|u^n \cdot \nabla \omega^n|^2 \leq C_K |\omega^n|^4$ . Moreover, since  $(u^n \cdot \nabla \omega^n, \omega^n) = 0$ , then

$$|\omega^n - h(u^n \cdot \nabla \omega^n)|^2 = |\omega^n|^2 + h^2 |u^n \cdot \nabla \omega^n|^2 \leq |\omega^n|^2 (1 + C_K h^2 |\omega^n|^2).$$

For  $h$  such that  $\nu \lambda_M h < 1$  we have  $e^{\nu \lambda_M h} < 3$ . It follows that

$$\begin{aligned} \left| \sum_{k \in \mathcal{K}} \frac{2g_k}{\nu|k|^2} (e^{\nu|k|^2 h} - 1) e^{ik \cdot x} \right| &= \left( 4\pi^2 \sum_{k \in \mathcal{K}} \frac{4|g_k|^2}{\nu^2 |k|^4} (e^{\nu|k|^2 h} - 1)^2 \right)^{1/2} \\ &\leq (e^{\nu \lambda_M h} - 1) \frac{2\|f\|}{\nu \lambda_0^{1/2}} \leq \nu \lambda_M h \frac{6\|f\|}{\nu \lambda_0^{1/2}}. \end{aligned}$$

Therefore,

$$\begin{aligned}
|\omega^{n+1}|^2 e^{2\nu\lambda_0 h} &\leq |\omega^n|^2 (1 + C_K h^2 |\omega^n|^2) \\
&\quad + 2|\omega^n| (1 + C_K h^2 |\omega^n|^2)^{1/2} \nu \lambda_M h \frac{6|f|}{\nu \lambda_0^{1/2}} \\
&\quad + \nu^2 \lambda_M^2 h^2 \frac{36|f|^2}{\nu^2 \lambda_0} \\
&\leq |\omega^n|^2 (1 + C_K h^2 |\omega^n|^2) (1 + \nu \lambda_0 h) \\
&\quad + \left( \frac{\lambda_M}{\lambda_0} + \nu \lambda_M h \right) \nu \lambda_M h \frac{36|f|^2}{\nu^2 \lambda_0}.
\end{aligned}$$

Now, if  $B \leq |\omega^n| \leq L$ , then

$$|\omega^{n+1}|^2 \leq \alpha(h) e^{-2\nu\lambda_0 h} |\omega^n|^2$$

where

$$\alpha(h) = (1 + C_K h^2 L^2) (1 + \nu \lambda_0 h) + 36 \left( \frac{\lambda_M}{\lambda_0} + \nu \lambda_M h \right) \frac{\nu \lambda_M h}{c_0^2}.$$

Since  $\alpha(h) \rightarrow 1$  as  $h \rightarrow 0$  and

$$\alpha'(0) = \nu \lambda_0 + 36 \frac{\nu \lambda_M^2}{c_0^2 \lambda_0} < 2\nu \lambda_0,$$

there is  $h$  small enough that  $\gamma = \alpha(h) e^{-2\nu\lambda_0 h} < 1$  as well as  $\nu \lambda_M h < 1$ . Let  $N$  be large enough that  $L\gamma^N < B$ . Since  $|\omega^n| < B$  implies  $|\omega^{n+1}|^2 \leq \gamma B^2 < B^2$ , once  $|\omega^n|$  falls below  $B$  it stays below  $B$ . It follows that  $|\omega^{n+1}| < B$  for all  $n \geq N$ , which completes the proof of the lemma. ■

Up to the constant  $c_0$ , the bound on  $B$  given above is the same as the usual estimate on the absorbing ball of the two-dimensional incompressible Navier–Stokes equations (10), see, for example [35]. Note that the estimate on the size of  $h$  depends on  $C_K$ , which we have not explicitly computed here. Lemma 1 is important theoretically; however, as with other *a priori* estimates of this type, the resulting bounds on  $h$  and  $B$  differ by many orders of magnitude from those suggested by the numerics. A similar theorem could be proved about the discrete alpha models. As only  $\omega^n$  is used when computing the residual  $\rho^n$ , we omit that theorem and proof.

Consider next the computation of the discrete residual. For the discrete dynamical systems given by (14) and (16) we obtain

$$\rho_k^{n+1} = \rho_k^n + h \left\{ (\bar{u}^n \cdot \nabla w^n)_k - (u^n \cdot \nabla w^n)_k \right\} e^{-\nu|k|^2 h}. \quad (17)$$

We remark again that, aside from the model error which we are trying to compute, the only error which enters into the computation of  $\rho^n$  comes from the rounding present in the floating-point arithmetic. As in the continuous case, the discrete residual velocity may be obtained from the residual vorticity. In particular,  $R_k^n = i\rho_k^n(k_2, -k_1)/|k|^2$ .

Note that  $R_k^n$  reflects the modeling error made when replacing our fully discrete dynamical system by a similarly discretized alpha model. Similar results should hold if other numerical schemes, such as BDF2, were used. The method described here could also be used to compute

the evolution of the residual error in other turbulence models. Moreover, it should be possible to track the residual error present in a particular discretization of a continuous dynamical system, for example, by comparing different numerical schemes. For work along these lines please see Banks, Hittinger, Connors and Woodward [1] and references therein. While it may be possible that similar techniques could be used to relate the discrete residuals  $R_k^n$  that we compute here to the model error in the fully-continuous alpha models, we do not pursue this direction of inquiry.

The computations which appear in this paper were implemented using the MIT/Intel Cilkplus parallel processing extensions to the C programming language and compiled using GCC version 5.1. The fast Fourier transforms used to compute the non-linear term were performed using the FFTW3 software library. All computations were carried out using IEEE 754 double-precision floating point on the PDE Wulf cluster and the UNR Grid at the University of Nevada Reno. The final computations presented here took a total of 38 400 core-hours of processing time using Intel Xeon E5-2650 CPUs. The Navier–Stokes solver described in [27] was used to verify the correctness of our computations.

The specific discretization considered here uses a  $256 \times 256$  spatial grid with  $K = 85$  and a time step of  $h = 25/4096$ . For practical reasons  $h$  has been taken to be many orders of magnitude larger than the bounds given in Lemma 1. Numerically, this choice of parameters leads to a stable numerical scheme with a Courant–Friedrichs–Lewy condition number of

$$\text{CFL} = \frac{Kh}{2\pi} \sup \{|u^n(x_{ij})|_1 : x_{ij} \in \Omega \text{ and } t_n \leq 100\,000\} \approx 0.18$$

where  $x_{ij} = 2\pi(i, j)/256$  and  $|(u_1, u_2)|_1 = |u_1| + |u_2|$ . We henceforth assume that (14) possesses a global attractor  $\mathcal{A}_{K,h}$  suitable for our study. Starting from the initial condition  $u^0(x) = 0$ , we obtain by time  $t = 25\,000$  a complex time-dependent velocity field whose statistical properties appear to have reached a steady state.

To further characterize the time scales in our computation, we estimate the eddy turnover time  $\tau$  using the definition of Gesho, Olson and Titi [16] as

$$\tau = 4\pi^2 \sum_{r=1}^{\infty} r^{-1} E(r) / \left( \sum_{r=1}^{\infty} E(r) \right)^{3/2} \approx 92.05,$$

where  $E(r)$ , see Figure 6, is the time-averaged energy spectrum given by

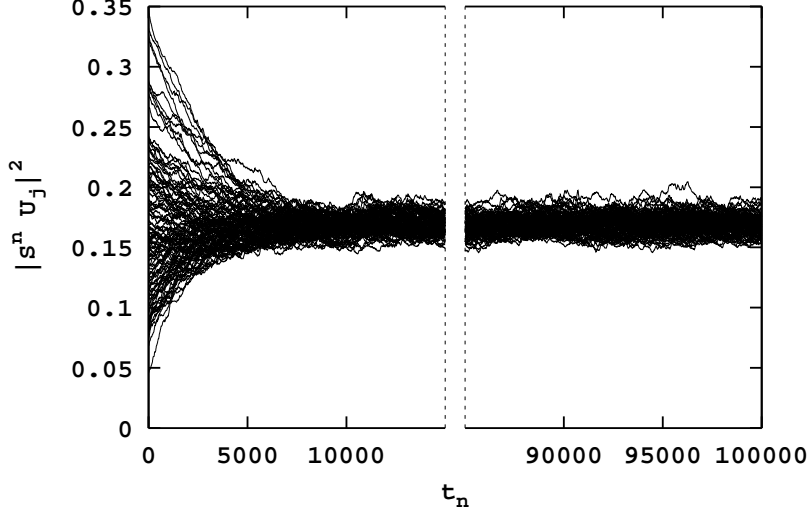
$$E(r) = \frac{4\pi^2}{T - T_0} \int_{T_0}^T \sum_{k \in \mathcal{J}_r} |u_k(t)|^2 dt$$

averaged from  $T_0 = 25\,000$  to  $T = 100\,000$  where

$$\mathcal{J}_r = \{k \in \mathbf{Z}^2 : r - 0.5 < |k| \leq r + 0.5\}.$$

Note that the flow undergoes an additional 814 eddy turnovers on this time interval. We presume, therefore, that  $u^n$  lies very near the global attractor of our discrete dynamical system for  $t_n \geq 100\,000$ . We now describe the discrete ensemble averages that will be used to compute the root-mean-squared residual error in our discrete alpha models.

Figure 4: Long-time evolution of 100 solutions of the two-dimensional Navier–Stokes equations with randomly chosen initial conditions leading to 100 different points on the attractor. Note that the graph has been broken and data omitted between times  $t_n = 15\,000$  and  $t_n = 85\,000$ .



The set  $\mathcal{U}$ , which forms the support of the probability measure  $\mu$  used to define our ensemble averages, was taken to consist of 100 points, each obtained by choosing a random velocity field  $U_j$  and then evolving that field forward  $T = 100\,000$  units in time. Figure 4 shows the evolution of  $\|S^n U_j\|_{L^2}^2$  for  $j = 1, 2, \dots, 100$ . The statistical properties of the energy appear to have reached a steady state by  $t_n = 25\,000$  and by time  $t_n = 100\,000$  each flow has undergone approximately 1000 large-eddy turnovers. We presume, for the same reasons as before, that each element of

$$\mathcal{U} = \{S^n U_j : j = 1, 2, \dots, 100 \text{ and } t_n = 100\,000\}$$

is near the discrete global attractor  $\mathcal{A}_{K,h}$ .

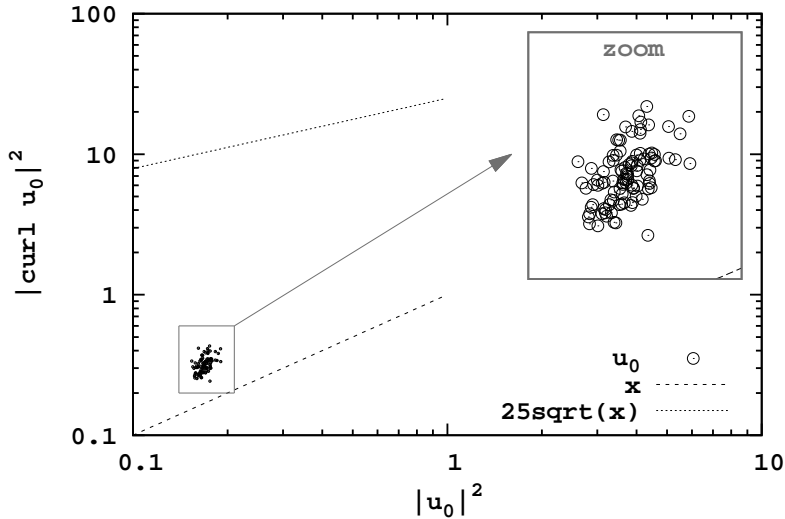
Before proceeding we further characterize the ensemble averages used in our computations. Figure 5 plots the points  $u_0 \in \mathcal{U}$  in the energy-ensrophy plane. The fact that all 100 points lie between the parabola and the line is consistent with the analysis of Dascaliuc, Foias and Jolly [9] on the location of the global attractor for the two-dimensional incompressible Navier–Stokes equations. Observe that the points are clustered together in a small region of the plane, but appear randomly distributed within that region.

The discrete ensemble averages may be defined as follows. For each  $u_0 \in \mathcal{U}$  let  $R_k^n(u_0)$  be the residual obtained by plugging the solution  $u_k^n$  with  $u^0 = u_0$  into (17). Take  $\mu$  in (6) to be the uniform probability measure supported on  $\mathcal{U}$ . It follows that

$$\mathcal{E}_{\text{rms}}^n = \langle \|R^n\|^2 \rangle^{1/2} = \left\{ \frac{4\pi^2}{|\mathcal{U}|} \sum_{u_0 \in \mathcal{U}} \sum_{k \in \mathcal{K}} |k|^2 |R_k^n(u_0)|^2 \right\}^{1/2} \quad (18)$$

where  $|\mathcal{U}| = 100$  denotes the cardinality of  $\mathcal{U}$ . Characterizing how  $\mathcal{E}_{\text{rms}}^n$  depends on  $t_n$  will be the main focus of the computational results in the next section.

Figure 5: Locations in the energy-ensrophy plane of the 100 points on the attractor  $u_0 \in \mathcal{U} \subseteq \mathcal{A}$  used for the ensemble averages.



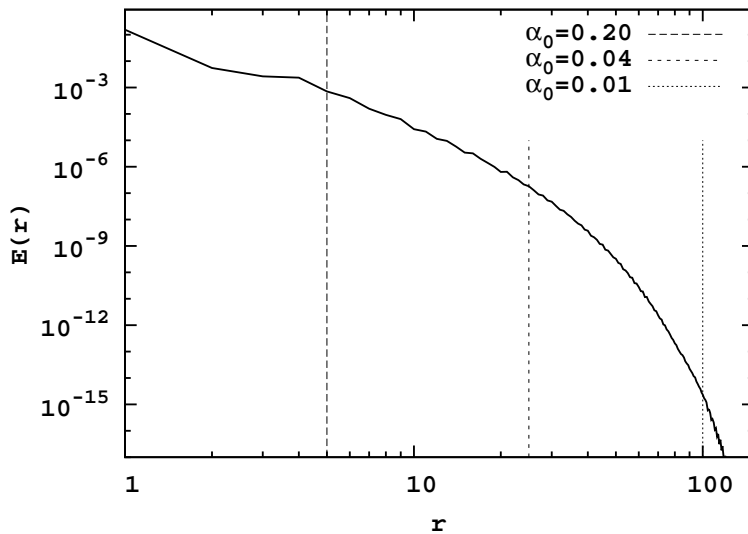
## 4 Computational Results

For our numerical study, we compute the root-mean-squared residual error for nine different turbulence models, determined by taking  $d$  and  $\alpha_0$  such that  $d \in \{0, 4, \infty\}$  and  $\alpha_0 \in \{0.01, 0.04, 0.20\}$ . Intuitively, for small values of  $\alpha_0$  we expect an alpha model to function as a subgrid-scale model [7, 22] and for large values of  $\alpha_0$  as a Reynolds stress closure [4, 5, 6]. To see how the different values of  $\alpha_0$  considered in our numerical experiments compare with the energetics of a typical flow on the global attractor of (14), Figure 6 plots the energy spectrum  $E(r)$  of the solution  $u^n$  with initial condition  $u^0 = 0$  averaged between times  $T_0 = 25\,000$  and  $T = 100\,000$  against the vertical lines  $|k| = 1/\alpha_0$ . Each of these vertical lines represent the wavenumber at which the Fourier modes are attenuated by 50 percent in the smoothing filter of the original LANS-alpha model. As previously illustrated in Figure 2, larger values of  $d$  lead to slightly less attenuation at this wavenumber. We remark that the smallest averaging length scale  $\alpha_0 = 0.01$  leads to smoothing filters affecting modes in the dissipation range of the energy spectrum, that  $\alpha_0 = 0.04$  also affects modes in the inertial range and that the relatively large value of  $\alpha_0 = 0.2$  affects all the modes including those in the forcing range and inverse cascade.

Before computing the ensemble averages defined by equation (18) it is informative to directly examine the residual error computed along a single representative trajectory lying on the global attractor. Let  $u_0 \in \mathcal{A}_{K,h}$  be fixed. Curves showing the evolution of the norm of  $R^n(u_0)$  for the nine different turbulence models studied are plotted in Figure 7. For  $\alpha_0 = 0.20$  the residual error is the largest and appears to grow linearly with time after  $t_n \geq 4000$  for each value of  $d$ . For  $\alpha_0 = 0.04$  the curves group together in the middle of the graph and appear to grow as  $\sqrt{t_n}$ . In this group the curve corresponding to  $d = 0$  deviates from the other two when  $t_n \geq 20000$  and starts to grow at a slightly faster rate. This deviation, though slight in the log-log plot, is significant as further numerics shall indicate. For  $\alpha_0 = 0.01$  the

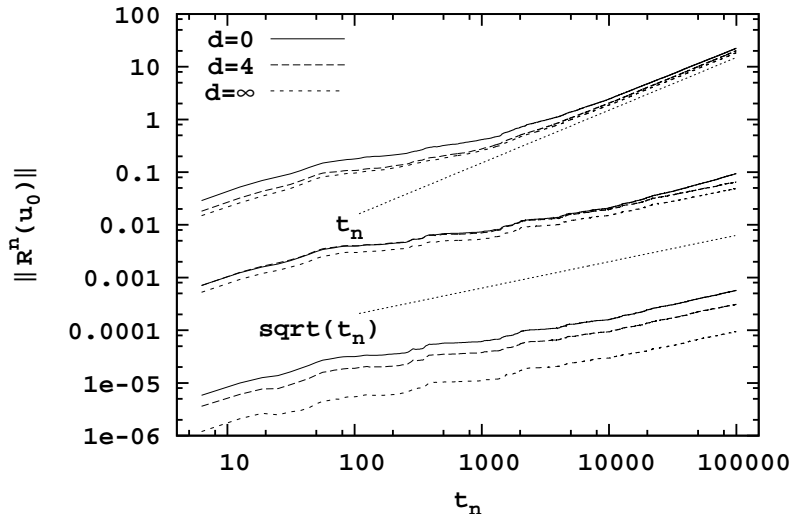


Figure 6: The average energy spectrum of  $u$  in relation to the wavenumbers  $|k| = 1/\alpha_0$  corresponding to three choices of  $\alpha_0$ .



residual error is the least and separate curves appear at bottom of the graph. Each of these curves appear to grow as  $\sqrt{t_n}$  over the entire range. Therefore, even without taking ensemble averages, the differences in the growth rates of the residual error described in our main result can be observed for the different turbulence models.

Figure 7: Evolution of the residual error along a single trajectory. The top three curves correspond to  $\alpha_0 = 0.20$ , the middle three to  $\alpha_0 = 0.04$  and the bottom three to  $\alpha_0 = 0.01$ . Values for  $d$  are as indicated.



Before proceeding to the computation of  $\mathcal{E}_{\text{rms}}^n$ , we verify that our ensemble averages satisfy the assumption (8) that  $\langle r'(t)^2 \rangle^{1/2}$  has a positive lower bound which is uniform in time. As

Table 1: Numerical lower bounds on  $\sup \{ \langle r'(t)^2 \rangle^{1/2} : \|\phi\| = 1 \}$  for  $t \in [0, T]$  where  $T = 100\,000$  obtained by taking  $\phi \in \{\phi_1, \phi_2, \phi_3\}$ .

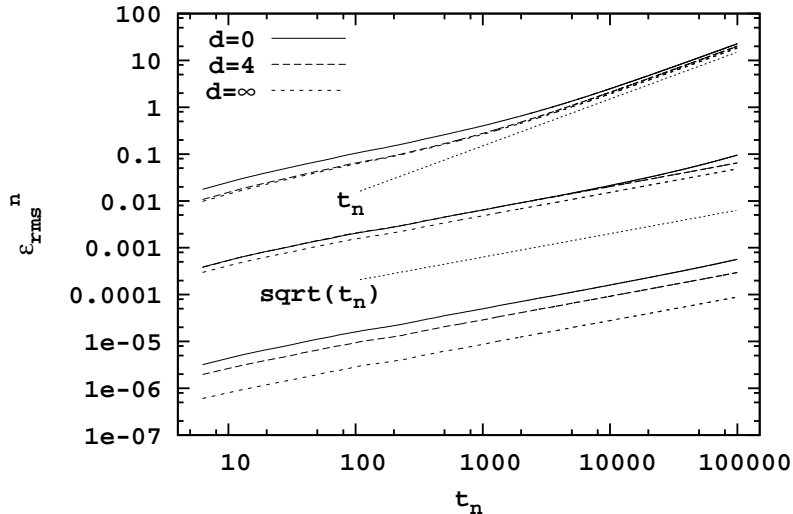
$\alpha_0$	$d$	$\phi_1$	$\phi_2$	$\phi_3$
0.01	0	$3.7383 \times 10^{-09}$	$3.7421 \times 10^{-09}$	$2.3073 \times 10^{-09}$
0.01	4	$9.3591 \times 10^{-10}$	$7.0558 \times 10^{-10}$	$5.1470 \times 10^{-10}$
0.01	$\infty$	$1.3167 \times 10^{-10}$	$1.1054 \times 10^{-10}$	$7.1270 \times 10^{-11}$
0.04	0	$6.9357 \times 10^{-07}$	$8.1933 \times 10^{-07}$	$4.0261 \times 10^{-07}$
0.04	4	$8.6752 \times 10^{-07}$	$5.9190 \times 10^{-07}$	$4.5601 \times 10^{-07}$
0.04	$\infty$	$5.5177 \times 10^{-07}$	$3.4297 \times 10^{-07}$	$2.6645 \times 10^{-07}$
0.2	0	$6.7480 \times 10^{-05}$	$2.0257 \times 10^{-04}$	$4.8341 \times 10^{-05}$
0.2	4	$4.5501 \times 10^{-05}$	$1.8437 \times 10^{-04}$	$3.5777 \times 10^{-05}$
0.2	$\infty$	$4.5846 \times 10^{-05}$	$1.6867 \times 10^{-04}$	$3.5809 \times 10^{-05}$

it is impossible to take the supremum over all values of  $\phi$  choose  $\phi \in \{\phi_1, \phi_2, \phi_3\}$  with

$$\phi_1 = \frac{P_H(u_0 \cdot \nabla u_0)}{\|P_H(u_0 \cdot \nabla u_0)\|}, \quad \phi_2 = \frac{f}{\|f\|} \quad \text{and} \quad \phi_3 = \frac{u_0}{\|u_0\|}. \quad (19)$$

Here  $u_0 = \text{curl}^{-1}\omega(T)$  where  $\omega$  is the solution depicted in Figure 3 at  $T = 100\,000$  and  $P_H$  is the  $L^2$  projection onto the divergence-free elements of  $V$ . The computational results given in Table 1 indicate that all three choices of  $\phi$  yield similar minimum values for  $\langle r'(t)^2 \rangle^{1/2}$  and that each of these are positive. Moreover, with one minor exception, the lower bounds on  $\langle r'(t)^2 \rangle^{1/2}$  decrease as both  $\alpha_0$  decreases and as  $d$  increases.

Figure 8: Evolution of  $\mathcal{E}_{\text{rms}}^n$  for nine different choices of parameters. The top three curves correspond to  $\alpha_0 = 0.20$ , the middle three to  $\alpha_0 = 0.04$  and the bottom three to  $\alpha_0 = 0.01$ . Values for  $d$  are as indicated.



We turn now to our main result, the computation of the root-mean-square residual error. Curves showing the evolution of  $\mathcal{E}_{\text{rms}}^n$  for  $d \in \{0, 4, \infty\}$  and  $\alpha_0 \in \{0.01, 0.04, 0.20\}$  are plotted in Figure 8. In this figure the curves appear smoother but are otherwise similar to those in Figure 7, especially for large values of  $t_n$ . To further characterize the growth of the residual error, we find a least squares fit for the parameters  $C_1$  and  $C_2$  such that

$$(\mathcal{E}_{\text{rms}}^n)^2 \approx C_2 t_n^2 + C_1 t_n.$$

If the residual error were comprised of a stochastic force plus a systematic bias, then comparing with (5) would allow us to estimate  $\text{Tr } Q \approx C_1$  and  $\|F_b\|^2 \approx C_2$ . Since the residual actually comes from a deterministic dynamical system, this is not the case. However, the intuitive notion that a good turbulence model should have an unbiased residual error implies that the term represented by  $C_2 t_n^2$  should be small compared to  $C_1 t_n$ . To characterize the relative size of these two terms at the end of each computational run we define the dimensionless ratio  $\eta = C_2 T / C_1$ .

Table 2 reports the values of  $C_1$ ,  $C_2$  and  $\eta$  for the computational runs given in Figure 8. When  $\alpha_0$  is fixed, the estimates of  $C_1$  and  $C_2$  have similar orders of magnitude for different values of  $d$  that generally decrease as  $d$  increases. The values of  $\eta$  are nearly the same when  $d = 4$  or  $d = \infty$  but differ when  $d = 0$ . It should be pointed out that, although  $\eta$  depends directly on the length  $T = 100\,000$  of the computational run, it is still meaningful to compare the relative sizes of  $\eta$  for different choices of  $\alpha_0$  and  $d$  while keeping  $T$  fixed.

Table 2: Least squares fit of  $(\mathcal{E}_{\text{rms}}^n)^2 \approx C_2 t_n^2 + C_1 t_n$  and the ratio  $\eta = C_2 T / C_1$  at the end of the computation when  $T = 100\,000$ .

$\alpha_0$	$d$	$C_1$	$C_2$	$\eta$
0.01	0	$2.513 \times 10^{-12}$	$7.086 \times 10^{-18}$	0.28
0.01	4	$8.489 \times 10^{-13}$	$2.733 \times 10^{-19}$	0.03
0.01	$\infty$	$7.723 \times 10^{-14}$	$1.698 \times 10^{-20}$	0.02
0.04	0	$4.066 \times 10^{-08}$	$5.010 \times 10^{-13}$	1.23
0.04	4	$4.108 \times 10^{-08}$	$1.100 \times 10^{-14}$	0.03
0.04	$\infty$	$2.306 \times 10^{-08}$	$2.747 \times 10^{-15}$	0.01
0.2	0	$1.179 \times 10^{-04}$	$5.019 \times 10^{-08}$	42.56
0.2	4	$4.175 \times 10^{-05}$	$3.985 \times 10^{-08}$	95.47
0.2	$\infty$	$4.319 \times 10^{-05}$	$3.358 \times 10^{-08}$	77.75

The similarity between the entries in Table 2 for  $d = 4$  and  $d = \infty$  is consistent with [33] wherein it is reported that for all tested applications  $d = 3$  already gives acceptable results, and that choosing  $d$  larger than 5 does not improve the results significantly. The value  $\alpha_0 = 0.20$  leads to  $\eta \gg 1$  for every choice of  $d$ , which suggests some sort of linearly growing bias dominates the residual error when  $\alpha_0$  is large. When  $\alpha_0 = 0.04$  and  $d = 0$  the time evolution of the residual error deviated slightly from the line  $\sqrt{t_n}$  in Figure 8. For this choice of parameters Table 2 indicates that  $\eta \approx 1.23$ . This means that by the end of the computational run the linearly growing part of the residual error contributes more than 50

percent to the total error. While the exact balance between the two terms depends on  $T$ , it is interesting that the value of  $\eta$  in the  $d = 0$  case differs from the  $d = 4$  and  $d = \infty$  cases by a couple orders of magnitude when  $\alpha_0 = 0.04$ . While the value  $\alpha_0 = 0.01$  leads to  $\eta < 1$  for every choice of  $d$ , it is again notable that  $d = 0$  leads to a larger  $\eta$ . We conclude by observing that  $\eta \ll 1$  implies the linearly growing term intuitively identified as bias is negligible over a time period of more than 1000 large-eddy turnovers and the residual error, though deterministic, behaves as if the model error were given by stochastic force. The next section provides additional analysis which clarifies this point and further characterizes the bias as well as the time and spatial correlations in the residual error.

## 5 Further Analysis

This section further characterizes the residual errors computed in the previous section. By expanding upon the previous section, our goal is to determine to what extent the deterministic model errors considered here behave as the spatially-correlated and temporally-white Gaussian processes employed in theoretical works on data assimilation such as [20].

Let us begin by examining the ensemble averages of the residual error

$$\langle \rho^n \rangle = \frac{1}{|\mathcal{U}|} \sum_{u_0 \in \mathcal{U}} \rho^n(u_0)$$

at the end of each computational run when  $t_n = 100\,000$ . Figure 9 illustrates four examples from the nine choices of parameters studied: two cases when  $\eta \ll 1$  and when  $\eta \gg 1$ . When  $\eta \ll 1$  the ensemble average of the residual error looks almost random. When  $\eta \gg 1$ , the ensemble average of the residual error looks remarkably like the forcing function depicted in Figure 3. While it is not surprising that the residual error has a bias around the body forcing when the averaging length scale is large, it is surprising that this bias is of opposite signs when  $d = 0$  compared to when  $d = 4$ . This change in sign suggests an alpha model may exist for some fractional value of  $d \in (0, 4)$  that minimizes the bias around the body forcing for large values of  $\alpha_0$ . Since taking  $\alpha_0$  large translates into computational savings, increasing the accuracy in this situation by removing bias could be of practical importance. Note that without taking ensemble averages the plots of  $\rho^n$  when  $t_n = 100\,000$  look essentially the same as those depicted for the ensemble averages in Figure 9. In particular, the sign differences between  $d = 0$  and  $d = 4$  when  $\alpha_0 = 0.2$  are consistent across all 100 independent trajectories considered in our study. Finally it is worth mentioning that the sign of the bias around the forcing function doesn't oscillate in time, but instead becomes more and more distinct.

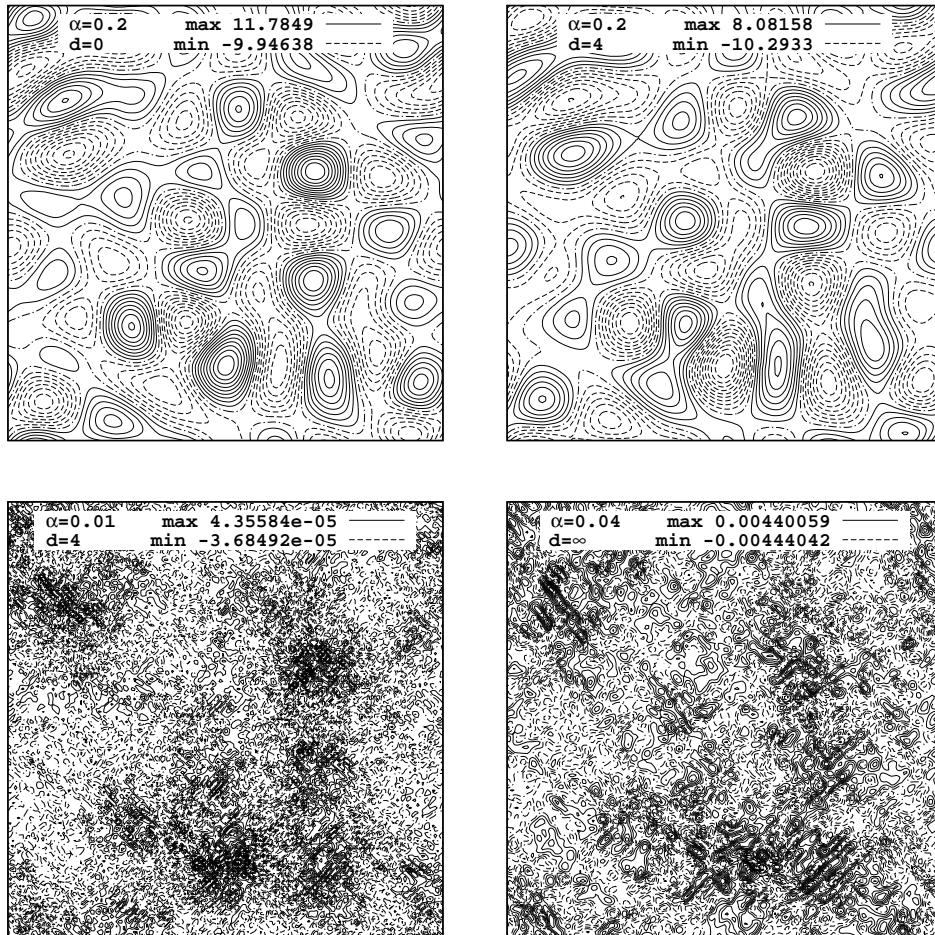
Now describe the degree to which the residual error consists of independent increments. Let  $\delta = 0.390625$  in (7) to obtain  $J = 256\,000$  time increments for every  $u_0 \in \mathcal{U}$  of the form  $z_j = ((Z_j, \phi))$  where

$$Z_j = R(\tau_j; u_0) - R(\tau_{j-1}; u_0) \quad \text{and} \quad \tau_j = j\delta.$$

Here  $\phi$  is a unit vector chosen as in (19). The resulting autocorrelations at the point  $(\phi, \phi)$  may be computed using the ratios  $\gamma(\Delta t)/\gamma(0)$  with  $\Delta t = \delta\ell$  and

$$\gamma(\Delta t) = \left\langle \frac{1}{J-\ell} \sum_{j=1}^{J-\ell} (z_j z_{j+\ell} - \bar{z}_0 \bar{z}_\ell) \right\rangle \quad \text{where} \quad \bar{z}_k = \left\langle \frac{1}{J-\ell} \sum_{j=1}^{J-\ell} z_{j+k} \right\rangle.$$

Figure 9: Contours of  $\langle \rho^n \rangle$  at time  $t_n = 100\,000$  for selected set of values for  $\alpha_0$  and  $d$ .

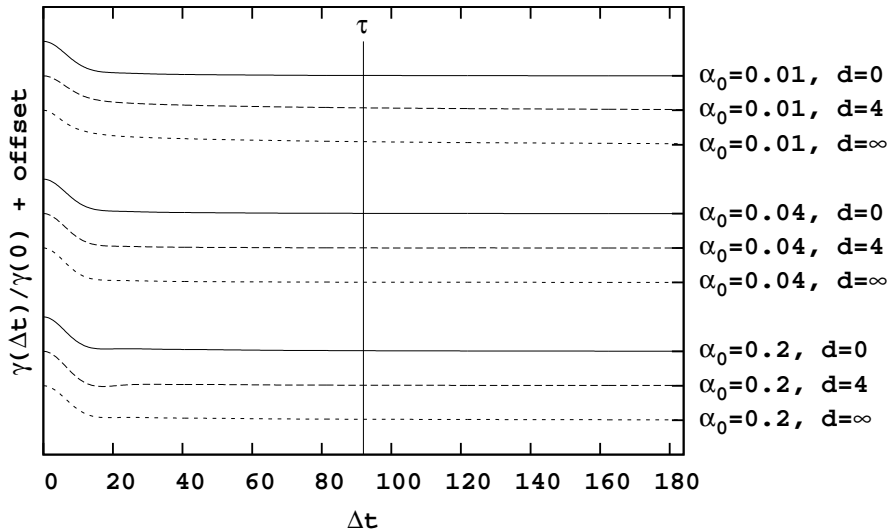


Computational results for the case  $\phi = \phi_2$  are depicted in Figure 10. We take  $\Delta t \in [0, 2\tau]$  where  $\tau$  is the time for one large-eddy turnover. Note that  $2\tau$  is small compared to total length of each time-series, which is greater than  $1000\tau$ . When  $\Delta t$  is small but positive, the autocorrelation is near unity, as expected from (9). As  $\Delta t$  increases the autocorrelation decreases. Table 3 characterizes the apparent support of the autocorrelation by computing the length of the smallest interval such that  $|\sigma(\Delta t)/\sigma(0)| < 0.05$  for all values of  $\Delta t$  outside that interval. When  $\alpha_0 = 0.04$  or  $\alpha_0 = 0.2$  the size of this interval is about  $\tau/4$ . When  $\alpha_0 = 0.01$  the size of the interval is noticeably larger. This is somewhat surprising given the slow growth of  $\mathcal{E}_{\text{rms}}^n$  in this case. Note that using a cutoff of 0.05 to describe the interval of support was somewhat arbitrary—other cutoffs reveal a similar relationship between the parameters  $\alpha_0$ ,  $d$ ,  $\phi$  and the size of the interval.

Next, characterize the spatial correlations in residual error. Working with the residual vorticity  $\rho$  is simpler than  $R$  because it is a scalar. Since the norm on  $V$  satisfies

$$\|R(t)\|^2 = \int_{\Omega} |\rho(t, x)|^2 dx,$$

Figure 10: Autocorrelation for  $\gamma(\Delta t)/\gamma(0)$  when  $\phi = \phi_2$ . The graphs have been offset along the vertical axis for clarity. The vertical line at  $\tau$  represents the time for one large-eddy turnover.



then working with  $\rho$  is also, in some sense, natural. For completeness, we also consider spatial correlations in residual velocity field  $R$  as well.

To begin, let  $\delta = 6.25$  to obtain  $J = 16\,000$  increments in the residual vorticity given by  $\zeta_j = \rho(\tau_j) - \rho(\tau_{j-1})$  where  $\tau_j = j\delta$ . Figure 11 illustrates the correlation  $\sigma(\Delta x)/\sigma(0)$  where

$$\sigma(\Delta x) = \left\langle \frac{1}{J} \sum_{j=1}^J \left( \zeta_j(\pi, \pi) \zeta_j(\pi + \Delta x, \pi) - \bar{\zeta}(\pi, \pi) \bar{\zeta}(\pi + \Delta x, \pi) \right) \right\rangle \quad (20)$$

and

$$\bar{\zeta}(x, y) = \left\langle \frac{1}{J} \sum_{j=1}^J \zeta_j(x, y) \right\rangle.$$

These curves may be seen as particular slices of the covariance matrix of the residual error in the vorticity at the point  $(\pi, \pi)$  corresponding to the  $x$ -axis. It is interesting that when  $\alpha_0 = 0.01$  and  $\alpha_0 = 0.04$  there is a distance  $\Delta x$  for which the correlation is negative. Nearly identical graphs are obtained when slicing the covariance matrix at different points in different directions. In particular, although the presence of a non-zero body force has the potential to render the statistics of the resulting flow neither homogeneous or isotropic, our results show that the spatial correlations of the residual error are nearly homogeneous and isotropic. This is consistent with the assumptions of homogeneity and isotropy used in the derivations of the turbulence models.

Note that the apparent support of the spatial correlations increases as  $\alpha_0$  increases but is less affected by  $d$ . Table 3 characterizes the support of the spatial correlation in a way analogous to the method used for the autocorrelation. For comparison, the support of the spatial correlations in the flow itself, obtained by taking  $\zeta_j = \omega(\tau_j) - \omega(\tau_{j-1})$  in (20), may be characterized by an interval of length 1.74 outside of which the correlation is less than 0.05.

Table 3: Lengths of the smallest intervals in time outside of which the autocorrelation  $|\gamma(\Delta t)/\gamma(0)| < 0.05$  for  $\phi \in \{\phi_1, \phi_2, \phi_3\}$  and the lengths of the smallest intervals in space outside of which the spatial correlations  $|\sigma(\Delta x)/\sigma(0)| < 0.05$  and  $|\text{Tr } \sigma_u(\Delta x)/\text{Tr } \sigma_u(0)| < 0.05$ .

$\alpha_0$	$d$	$\phi_1$	$\phi_2$	$\phi_3$	$\sigma$	$\text{Tr } \sigma_u$
0.01	0	17.97	34.38	87.50	0.49	0.74
0.01	4	19.92	119.92	150.39	0.39	0.39
0.01	$\infty$	22.27	141.41	86.72	0.39	0.39
0.04	0	19.14	28.52	54.69	0.64	0.76
0.04	4	17.19	22.27	38.28	0.74	0.61
0.04	$\infty$	14.84	25.78	39.45	0.66	0.47
0.2	0	23.83	46.09	43.75	1.08	1.94
0.2	4	13.67	12.89	14.45	1.01	2.38
0.2	$\infty$	28.52	53.52	40.23	1.64	2.38

We conclude the vorticity field of the original flow is spatially correlated over distances which are three to six times longer than the spatial correlations observed in the residual vorticity when  $\alpha_0 = 0.01$  and  $\alpha_0 = 0.04$ . When  $\alpha_0 = 0.2$  the distances are comparable.

This section finishes by characterizing the spatial correlations of the residual error in the velocity. To avoid the 2-by-2 matrices which arise from the horizontal and vertical components of  $R$ , take the trace to obtain

$$\text{Tr } \sigma_u(\Delta x) = \left\langle \frac{1}{J} \sum_{j=1}^J \left( R_j(\pi, \pi) \cdot R_j(\pi + \Delta x, \pi) - \bar{R}(\pi, \pi) \cdot \bar{R}(\pi + \Delta x, \pi) \right) \right\rangle.$$

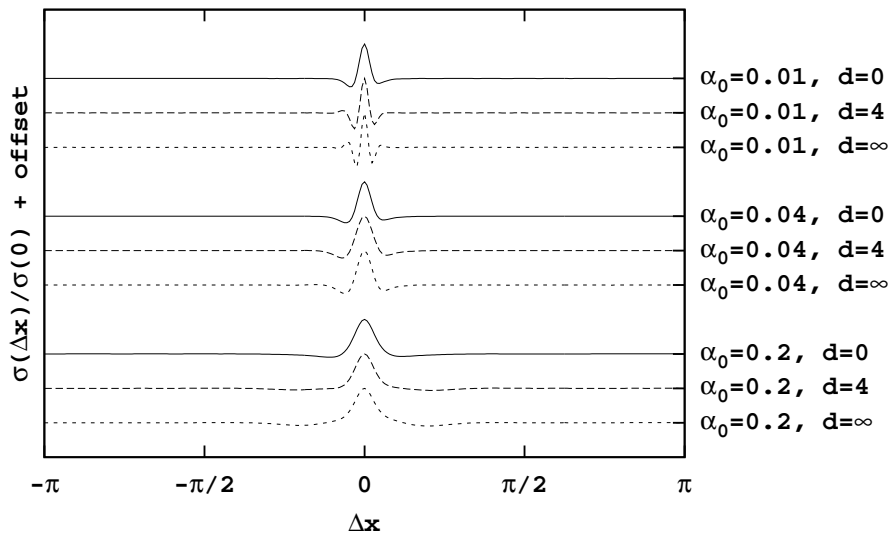
The graphs of  $\text{Tr } \sigma_u(\Delta x)/\text{Tr } \sigma_u(0)$  look similar to those in Figure 11 except with less compact support. This fact is quantified by the last column of Table 3. As with the vorticity, the correlation distances in the velocity field of the physical flow are three to six times longer than the correlation distances in the model error when  $\alpha_0 = 0.01$  and  $\alpha_0 = 0.04$ .

## 6 Conclusions and Future Work

A computational method was developed for studying the model error by calculating the time evolution of the root-mean-squared residual error taken over an ensemble of trajectories on the global attractor. We emphasize that the method of computing the model error employed in this paper avoids the difficulty that there is no shadowing result which can be used to compare separate evolutions of approximate dynamics to exact dynamics over long periods of time. Taking the discrete dynamics given by  $S$  to be exact allows us to focus on the effects of the alpha modeling apart from issues relating to the numerical discretization of the continuous dynamics.

During our study we identified an effective averaging length scale  $\alpha_0 = \alpha/\sqrt{d+1}$  in the LANS-alpha and NS-alpha deconvolution models of turbulence and created a new tur-

Figure 11: Spatial correlation  $\sigma(\Delta x)/\sigma(0)$  for different values of  $\alpha_0$  and  $d$ . The graphs have been offset along the vertical axis for clarity.



bulence model, the exponential-alpha model, corresponding to the limit as  $d \rightarrow \infty$ . This identification of  $\alpha_0$  allows direct comparison of the residual error while holding the behavior in the microscales essentially constant. Numerical computation showed for a particular time-independent forcing function with Grashof number  $G = 250\,000$  that

- if  $\alpha_0 = 0.01$  or if  $\alpha_0 = 0.04$  and  $d \in \{4, \infty\}$ , then  $\mathcal{E}_{\text{rms}}^n$  grows as  $\sqrt{t_n}$ ;
- if  $\alpha_0 = 0.20$  or if  $\alpha_0 = 0.04$  and  $d = 0$ , then  $\mathcal{E}_{\text{rms}}^n$  grows linearly as  $t_n$ .

Note that the NS-alpha deconvolution model of order  $d = 4$  performs similarly to the exponential-alpha model in these experiments. Little difference is expected, therefore, between NS-alpha deconvolution models with  $d \geq 4$ .

Although the residual errors in the deterministic alpha models are differentiable and do not have independent increments, when  $\alpha_0$  is sufficiently small they produce time series which are similar to a spatially-correlated and temporally-white Gaussian process. At the same time, when  $\alpha_0$  is too large, the model error includes a systematic bias. Further analysis indicates that this systematic bias is concentrated in a direction spanned by the forcing function. Moreover, when  $d = 0$  the bias is opposite in sign compared to when  $d = 4$ . This suggests for large values of  $\alpha_0$  that there may exist a fractional value of  $d \in (0, 4)$  which removes the bias and for which  $\mathcal{E}_{\text{rms}}^n$  grows as  $\sqrt{t_n}$ .

It would be interesting to further study the analytic properties of the new exponential alpha model proposed in this paper, to use the effective averaging length scale  $\alpha_0$  to compare subgrid scale models and boundary layers for flows with more complicated boundary conditions, to study how the body forcing affects the homogeneity and isotropy of the statistics of a turbulent flow and to use the techniques developed in this paper to create computationally efficient turbulence models with model errors that grow only as  $\sqrt{t}$  over time.



## Acknowledgements

The author was supported in part by NSF grant DMS-1418928. The author would like to thank the anonymous referees for many comments which improved this paper. One idea particularly worth mentioning was to increase the size of the ensemble averages and perform the statistical analysis given in Section 5.

## References

- [1] J. Banks, J. Hittinger, J. Connors, C. Woodward, A posteriori error estimation via nonlinear error transport with application to shallow water. *Recent Adv. in Scientific Comp. and App.*, Contemp. Math., vol. 586, Amer. Math. Soc., 2013, pp. 35–42,
- [2] G. Box, G. Jenkins, G. Reinsel, G. Ljung, *Time Series Analysis: Forecasting and Control*, 5th edition, Wiley, 2015, pp. 1–712.
- [3] Y. Cao, E.S. Titi, On the rate of convergence of the two-dimensional  $\alpha$ -models of turbulence to the Navier–Stokes equations. *Numer. Funct. Anal. Optim.*, vol. 30, no. 11–12, 2009, pp. 1231–1271.
- [4] S. Chen, C. Foias, D.D. Holm, E. Olson, E.S. Titi, S. Wynne, The Camassa–Holm equations as a closure model for turbulent channel and pipe flow, *Phys. Rev. Lett.*, vol. 81, 1998, pp. 5338–5341.
- [5] S. Chen, C. Foias, D.D. Holm, E. Olson, E.S. Titi, S. Wynne, A connection between the Camassa–Holm equations and turbulent flows in pipes and channels, *Phys. Fluids.*, vol. 11, 1999, pp. 2342–2353.
- [6] S. Chen, C. Foias, D.D. Holm, E. Olson, E.S. Titi, S. Wynne, The Camassa–Holm equations and turbulence, *Physica D*, vol. 133, 1999, pp. 49–65.
- [7] S. Chen, D.D. Holm, L.G. Margolin, R. Zhang, Direct numerical simulations of the Navier–Stokes alpha model, *Physica D*, vol. 133, 1999, pp. 66–83.
- [8] A. Cheskidov, Boundary layer for the Navier–Stokes-alpha model of fluid turbulence. *Arch. Ration. Mech. Anal.*, vol. 172, no. 3, 2004, pp. 333–362.
- [9] R. Dascaliuc, C. Foias, M.S. Jolly, Relations between energy and enstrophy on the global attractor of the 2-D Navier–Stokes equations, *J. Dynam. Differential Equations*, vol 17, no. 4, 2005, pp. 643–736.
- [10] G. Deugoué, P.A. Razafimandimby, Mamadou Sango, On the 3-D stochastic magneto-hydrodynamic- $\alpha$  model. *Stochastic Process. Appl.*, vol. 122, no. 5, 2012, pp. 2211–2248.
- [11] A. Dunca, Y. Epshteyn, On the Stolz–Adams deconvolution model for the large-eddy simulation of turbulent flows, *SIAM J. Math. Anal.*, vol. 37, no. 6, 2006, pp. 1890–1902.

- [12] C. Foias, R. Temam, Gevrey class regularity for the solutions of the Navier-Stokes equations, *J. Funct. Anal.*, vol. 87, no. 2, 1989, pp. 359–369.
- [13] C. Foias, D.D. Holm, E.S. Titi, The Navier–Stokes-alpha model of fluid turbulence, *Physica D*, vol. 152, 2001, pp. 505–519.
- [14] C. Foias, D.D. Holm, E.S. Titi, The three dimensional viscous Camassa–Holm Equations and their relation to the Navier–Stokes equations and turbulence theory, *Journal of Dynamics and Differential Equations*, vol. 14, 2002, pp. 1–35.
- [15] C. Foias, M.S. Jolly, R. Lan, R. Rupam, Y. Yang, B. Zhang, Time analyticity with higher norm estimates for the 2D Navier–Stokes equations, *IMA Journal of Applied Mathematics*, vol. 80, 2015, pp. 766–810.
- [16] M. Gesho, E. Olson, E.S. Titi, A computational study of a data assimilation algorithm for the two-dimensional Navier–Stokes equations, *Communications in Computational Physics*, vol. 10, no. 4, 2016, pp. 1094–1110.
- [17] B.J. Geurts, D.D. Holm, Leray and LANS- $\alpha$  modelling of turbulent mixing, *J. Turbul.*, vol. 7, 2006, pp. 10–33.
- [18] M.W. Hecht, D.D. Holm, M.R. Petersen, B.A. Wingate, The LANS- $\alpha$  and Leray turbulence parameterizations in primitive equation ocean modeling, *J. Phys. A*, vol. 41 no. 34, 2008, pp. 344009–344023.
- [19] T.J. Hui, Testing for Random Walk Hypothesis with or without Measurement Error, Masters Thesis, Imperial College London, 2012.
- [20] V.H. Hoang, K.J.H. Law, A.M. Stuart, Determining white noise forcing from Eulerian observations in the Navier-Stokes equation, *Stoch. Partial Differ. Equ. Anal. Comput.*, vol. 2, no. 2, 2014, pp. 233–261.
- [21] A.A. Ilyin, E.S. Titi, Attractors for the two-dimensional Navier-Stokes- $\alpha$  model: an  $\alpha$ -dependence study. *J. Dynam. Differential Equations* 15, no. 4, 2003, pp. 751–778.
- [22] T. Kim, M. Neda, L.G. Rebholz, Eliot Fried, A numerical study of the Navier–Stokes- $\alpha\beta$  model, *Comput. Methods Appl. Mech. Engrg.*, vol. 200, 2011, pp. 2891–2902.
- [23] A.Q. Lo, A.C. MacKinley, Stock market prices do not follow random walks: Evidence from a simple specification test, *The Review of Financial Study*, vol. 1, 1988, pp. 41–66.
- [24] M.C. Lopes Filho, H.J. Nussenzveig Lopes, E.S. Titi, A. Zang, Convergence of the 2D Euler- $\alpha$  to Euler equations in the Dirichlet case: indifference to boundary layers, *Phys. D* 292/293, 2015, pp. 51–61.
- [25] J.E. Marsden, S. Shkoller, The anisotropic Lagrangian averaged Euler and Navier-Stokes equations, *Arch. Ration. Mech. Anal.* vol. 166, no. 1, 2003, pp. 27–46.

- [26] P.D. Mininni, D.C. Montgomery, A.G. Pouquet, A numerical study of the alpha model for two-dimensional magnetohydrodynamic turbulent flows, *Phys. Fluids*, vol. 17, 2005, pp. 35112–35117.
- [27] E. Olson, E.S. Titi, Determining modes for continuous data assimilation in 2D turbulence. *J. Statist. Phys.*, vol. 113, no. 5-6, 2003, pp. 799–840.
- [28] L.G. Rebholz, A family of new, high order NS- $\alpha$  models arising from helicity correction in Leray turbulence models, *Journal of Mathematical Analysis and Applications*, vol. 342, 2008, pp. 246–254.
- [29] A.N. Komogorov, The local structure of turbulence in incompressible fluid for very large Reynolds numbers, *Dokl. Akad. Nauk SSSR.*, vol. 30, no. 4, 1941, pp. 301–305.
- [30] R.H. Kraichnan, Inertial ranges in two-dimensional turbulence, *Phys. Fluids*, vol. 10, 1967, pp. 1417–1423.
- [31] S. Kurien, K. Aivalis and K. Sreenivasan, Anisotropy of small-scale scalar turbulence, *J. Fluid Mech.*, vol. 448, 2001, pp. 279–288.
- [32] J.C. Sprott, *Chaos and Time-Series Analysis*, first edition, Oxford University Press, 2001, pp. 1–507.
- [33] S. Stolz, N.A. Adams, and D. Kleiser, An approximate deconvolution model for large-eddy simulation with application to incompressible wall-bounded flows, *Phys. Fluids*, vol. 13, 2001, pp. 997–1015.
- [34] M.A. Taylor, S. Kurien and G.L. Eyink, Recovering isotropic statistics in turbulence simulations: The Kolmogorov 4/5th- Law, *Phys. Rev. E*, vol. 68, 2003, pp. 26–31.
- [35] R. Temam, *Navier–Stokes equations and nonlinear functional analysis*, second edition, CBMS-NSF Regional Conference Series in Applied Mathematics, Vol. 66. Society for Industrial and Applied Mathematics, 1995, pp. 1–141.
- [36] Y. Xiao, Z. Xin, On 3D Lagrangian Navier–Stokes  $\alpha$  model with a class of vorticity-slip boundary conditions. *J. Math. Fluid Mech.*, vol. 15, no. 2, 2013, pp. 215–247.